

## Process-Oriented Diagnosis of Tropical Cyclones in High-Resolution GCMs

DAEHYUN KIM,<sup>a</sup> YUMIN MOON,<sup>a</sup> SUZANA J. CAMARGO,<sup>b</sup> ALLISON A. WING,<sup>c</sup>  
ADAM H. SOBEL,<sup>b,d</sup> HIROYUKI MURAKAMI,<sup>e,f</sup> GABRIEL A. VECCHI,<sup>f</sup> MING ZHAO,<sup>e</sup>  
AND ERIC PAGE<sup>a</sup>

<sup>a</sup> Department of Atmospheric Sciences, University of Washington, Seattle, Washington

<sup>b</sup> Lamont-Doherty Earth Observatory, Columbia University, Palisades, New York

<sup>c</sup> Department of Earth, Ocean, and Atmospheric Science, Florida State University, Tallahassee, Florida

<sup>d</sup> Department of Applied Physics and Applied Mathematics, Columbia University, New York, New York

<sup>e</sup> NOAA/Geophysical Fluid Dynamics Laboratory, Princeton, New Jersey

<sup>f</sup> Princeton University, Princeton, New Jersey

(Manuscript received 24 April 2017, in final form 6 November 2017)


### ABSTRACT

This study proposes a set of process-oriented diagnostics with the aim of understanding how model physics and numerics control the representation of tropical cyclones (TCs), especially their intensity distribution, in GCMs. Three simulations are made using two 50-km GCMs developed at NOAA's Geophysical Fluid Dynamics Laboratory. The two models are forced with the observed sea surface temperature [Atmospheric Model version 2.5 (AM2.5) and High Resolution Atmospheric Model (HiRAM)], and in the third simulation, the AM2.5 model is coupled to an ocean GCM [Forecast-Oriented Low Ocean Resolution (FLOR)]. The frequency distributions of maximum near-surface wind near TC centers show that HiRAM tends to develop stronger TCs than the other models do. Large-scale environmental parameters, such as potential intensity, do not explain the differences between HiRAM and the other models. It is found that HiRAM produces a greater amount of precipitation near the TC center, suggesting that associated greater diabatic heating enables TCs to become stronger in HiRAM. HiRAM also shows a greater contrast in relative humidity and surface latent heat flux between the inner and outer regions of TCs. Various fields are composited on precipitation percentiles to reveal the essential character of the interaction among convection, moisture, and surface heat flux. Results show that the moisture sensitivity of convection is higher in HiRAM than in the other model simulations. HiRAM also exhibits a stronger feedback from surface latent heat flux to convection via near-surface wind speed in heavy rain-rate regimes. The results emphasize that the moisture–convection coupling and the surface heat flux feedback are critical processes that affect the intensity of TCs in GCMs.

### 1. Introduction

Since the 1970s, it has been well known that global climate models (GCMs) are able to simulate vortices with characteristics similar to tropical cyclones (TCs; Manabe et al. 1970; Camargo and Wing 2016). As GCMs are also able to reproduce the relationship between TCs and El Niño–Southern Oscillation (ENSO), they have been used to develop dynamical TC seasonal forecasts (Vitart and Stockdale 2001; Camargo and Barnston

2009). More recently, with the aid of rapid increases in computing power, high-resolution GCMs with grid spacing of 20–50 km have been widely used in research and forecasting (e.g., Roberts et al. 2015; Wehner et al. 2017). Such higher-resolution global models reproduce the response of TCs to ENSO significantly better than older, lower-resolution GCMs (e.g., Zhang et al. 2016), leading to seasonal forecasts of regional (as opposed to only basinwide) TC activity; these forecasts include category 4 and 5 storms (not captured in older global models), as well as subseasonal TC forecasts (Vecchi et al. 2014; Murakami et al. 2015, 2016; Vitart et al. 2010). GCMs have also been used to make projections of future changes in TC activity using low resolution (Bengtsson et al. 1996; Camargo 2013) and high resolution (e.g., Manganello et al. 2014; Bacmeister et al. 2018), as

 Denotes content that is immediately available upon publication as open access.

Corresponding author: Daehyun Kim, daehyun@uw.edu

discussed in recent reviews (Knutson et al. 2010; Walsh et al. 2016).

The reliability of predictions and projections of future TC activity based on GCM simulations is affected by the degree to which the GCMs realistically capture the essential features of TC activity. Some GCMs are able to reproduce the observed temporal and geographical distribution of TC genesis and tracks, especially when forced with the observed sea surface temperature (SST; e.g., Zhao et al. 2009). Nonetheless, models exhibit a wide spectrum in their ability to reproduce the observed TC climatology, whether their horizontal resolutions are low (Camargo et al. 2005; Camargo 2013) or high (e.g., Shaevitz et al. 2014). This is true for multiple TC characteristics, but especially for TC intensity. Low-resolution global models have tended to simulate only the lower portion of the observed intensity distribution, lacking strong (i.e., category 4 or 5) TCs. This situation tends to improve as model resolution increases (Manganello et al. 2012), but not uniformly so (Roberts et al. 2015). A large spread in TC intensity distributions can occur in ensembles of models with similar or identical horizontal resolutions (Shaevitz et al. 2014), suggesting that factors other than horizontal resolution also affect simulated TC intensity. For example, Murakami et al. (2012a) showed that replacing the cumulus convection scheme in a GCM largely changed the simulation of global TC distribution, mean TC intensity, and temporal variation of TC frequency, even though the horizontal resolution remained the same. Also, studies have documented the sensitivity of simulated TC intensity to aspects of the dynamical core (e.g., Zhao et al. 2012; Reed et al. 2015) and to the ocean–atmosphere coupling grids (Zarzycki et al. 2016).

Modeling studies of TC activity often use relationships between the large-scale environment and TC characteristics to explain features of the simulations, basing their arguments on relationships between environmental parameters and TC activity in observations. For example, Wing et al. (2007) and Kossin and Camargo (2009) found that variations in the distribution of observed TC intensity were associated with variations in the theoretical maximum potential intensity (PI; Emanuel 1988) in the storms' environments. Building on these observational findings, the PI has been used to explain differences in TC intensity distributions in different model simulations (e.g., Camargo 2013; Camargo et al. 2016). Tropical cyclone genesis indices, which encapsulate empirically determined local relationships between the probability of tropical cyclone genesis and large-scale environmental variables (e.g., Gray 1979; Emanuel and Nolan 2004; Emanuel 2010; Tippett et al. 2011; Menkes et al. 2012), have also been used to explain

differences between model simulations of TC frequency (e.g., Camargo et al. 2007) and even (with some care, in a perfect model context) the response of TC frequency to the radiatively forced climate change (Camargo et al. 2014).

Explanations of simulated TC characteristics in terms of large-scale environmental variables alone tend to be most successful when addressing differences between different simulations with the same model. The differences in PI, genesis indices, vertical shear, and other environmental factors tend to be much too small to explain the large spread in TC characteristics found in multimodel ensembles, suggesting that differences between models are primarily due to differences in how each model's simulated TCs respond to their environments rather than differences in the environments themselves (e.g., Camargo et al. 2007). In other words, the relationship between TC characteristics and their large-scale environment is model dependent. To understand differences in TC characteristics between different models, it seems wisest to focus on differences in the interaction between their modeled TCs and large-scale environment. If two models, for example, employ two different convection schemes that exhibit vastly different sensitivities to environmental moisture, the two models could show a considerable difference in their TC characteristics even under similar large-scale environmental conditions.

Several investigators have examined interactions between the large-scale environment and model physics in studies of TCs in global models (Vitart et al. 2001; Reed and Jablonowski 2011; Murakami et al. 2012b; Stan 2012; Zhao et al. 2012; Kim et al. 2012; Lim et al. 2015; Duvel et al. 2017). Vitart et al. (2001) found that the characteristics of TCs in a GCM were particularly sensitive to a parameter in the deep convection scheme that controls the degree to which the deep convection is inhibited and suggested that the background model convective available potential energy (CAPE) is particularly relevant to explain these differences, even if that is not the case in observations. Zhao et al. (2012) similarly controlled the degree to which parameterized deep convection is suppressed by varying the lateral mixing rate. They found that a suppression of deep convection destabilizes the tropical atmosphere and thereby promotes stronger grid-scale mean vertical motion over the TC genesis area. It was suggested that stronger grid-scale mean vertical motion provides a favorable condition for TC development and intensification. Stan (2012) compared a conventional convective parameterization to a "super parameterization" in a climate model and showed that the explicit cloud process representation in the latter leads to more frequent, intense,

and long-lived TCs due to an increased moistening in the lower troposphere. [Lim et al. \(2015\)](#) showed that changes in the Emanuel and Nolan genesis potential index (GPI), which is a function of PI as well as other variables, are consistent with changes in TC intensity among the simulations of a single model when varying the minimum entrainment threshold in the convection scheme. While these modeling studies reveal statistical relationships between parameters in the convection scheme and TC activity, understanding of the mechanisms behind this relationship has remained incomplete, reflecting a lack of understanding of how deep convection and TCs are connected in climate models.

The current study proposes a set of process-oriented diagnostics that aim to explain the intermodel spread in TC intensity distribution. With the process-oriented diagnostics, we aim to provide deeper insights into parameterization features that are responsible for representation of TCs in GCMs. The close connection to parameterizations is a unique characteristic of the process-oriented diagnostics and reflects the explicit intent to assist model development. The ability of our proposed diagnostics to distinguish models with relatively intense TCs from models with relatively weak TCs will be tested by applying them to simulations made using two high-resolution GCMs in three different simulations. It will be shown that one GCM forced by the observed SSTs simulates stronger TCs than the other model (coupled or uncoupled) and that our process-oriented diagnostics shed light on the mechanisms behind the difference.

The paper is organized as follows. [Section 2](#) presents brief descriptions of the high-resolution models used in this study and the composite method. The process-oriented TC diagnostics will be introduced in [section 3](#), with their applications to the GFDL models. [Section 4](#) gives a summary of the results and conclusions.

## 2. Models and methods

### *a. GFDL high-resolution GCMs*

Two atmosphere-only GCMs—Atmospheric Model version 2.5 (AM2.5; [Delworth et al. 2012](#)) and the High Resolution Atmospheric Model (HiRAM; [Zhao et al. 2009](#))—and one ocean–atmosphere coupled GCM—Forecast-Oriented Low Ocean Resolution (FLOR; [Vecchi et al. 2014](#)) version of Coupled Model 2.5 (CM2.5; [Delworth et al. 2012](#))—developed at the Geophysical Fluid Dynamics Laboratory (GFDL) are used in this study. AM2.5 is the atmospheric component of CM2.5 and FLOR. FLOR is a descendent of CM2.5 developed for regional climate prediction by employing

an improved land model and a coarser resolution for the ocean and the sea ice models. HiRAM branched out from AM2.1, an ancestor of AM2.5, with the replacement of the convection and cloud scheme ([Zhao et al. 2009](#)). AM2.5 and FLOR use a relaxed Arakawa–Schubert scheme ([Moorthi and Suarez 1992](#)). The convection scheme in HiRAM was originally developed to simulate shallow convection with a constraint on the top of convective clouds ([Bretherton et al. 2004](#)). The restriction is removed when the scheme is implemented in HiRAM, and the scheme is allowed to simulate both deep and shallow convection ([Zhao et al. 2012](#)). Both AM2.5 and HiRAM use the finite-volume dynamical core ([Lin 2004](#)) on a cubed-sphere grid topology ([Putman and Lin 2007](#)). They use the same divergence damping coefficient [ $d_0$  in [Zhao et al. \(2012\)](#) is set to 0.16]. Both models also use the same time steps and physics–dynamics coupling interval: the gravity wave and advective (i.e., dynamics) and physics time steps are 200, 600, and 1200 s, respectively, while the radiation is called in every 3 h. In FLOR, the ocean–atmosphere coupling interval is 1 h. Further details of AM2.5, FLOR, and HiRAM can be found in [Delworth et al. \(2012\)](#), [Vecchi et al. \(2014\)](#), and [Zhao et al. \(2009\)](#), respectively.

All three GCMs are run at a 50-km horizontal resolution with the same 32 vertical levels in the atmosphere. The ocean GCM employed in FLOR is run at  $1^\circ \times 1^\circ$  horizontal resolution, telescoping to  $1/3^\circ$  meridional spacing near the equator with 50 vertical levels. The observed SST is prescribed as the boundary condition for AM2.5 and HiRAM, while the FLOR SSTs are calculated interactively by its oceanic component model and restored toward the observed SSTs with a 5-day nudging time scale to keep the model mean state close to observed. In this sense, in FLOR, the atmosphere and ocean are semicoupled. From a long-term (over 20 years) simulation made using each model, a period of 2 years (1984–85) is chosen for the current study. Note that the TC statistics in the select period are typical of each model. GCM outputs are saved with a 6-h time interval at the models' native grids and later interpolated to pressure levels for our analysis.

### *b. TC detection algorithm*

TC-like vortices are detected and tracked from the model fields using the tracking algorithm described in detail in [Murakami et al. \(2015\)](#). The tracking scheme mainly uses local sea level pressure minimum and warm-core conditions to detect TCs and impose a 3-day duration threshold on total lifetime, a 2-day threshold on warm-core condition, and a 36-h threshold on the warm core plus maximum 10-m near-surface winds greater

than  $15.75 \text{ m s}^{-1}$ . The tracking algorithm produces, for each TC, a time series of the TC's center longitude and latitude, minimum sea level pressure ( $\text{SLP}_{\min}$ ), and maximum surface wind speed ( $\text{WS}_{\max}$ ).

For the 2-yr period chosen, the tracking schemes identified 152, 191, and 247 TCs in the AM2.5, FLOR, and HiRAM simulations, respectively. Note that TCs with  $\text{SLP}_{\min}$  lower than 990 hPa at the time of the first detection, which in most cases occur in the midlatitudes, are excluded from our analysis. TCs whose latitudes are poleward of  $25^{\circ}\text{N}$  and  $25^{\circ}\text{S}$  at the time of the first detection are also excluded from the analysis. FLOR produces a relatively larger number of TCs than the other two models in the 2-yr period chosen for this study, reflecting the higher number of storms in that model's climatology.

### c. TC composites

The purpose of the TC composite analysis is to compare the structures of the simulated TCs among the three GFDL high-resolution models. It is important that the model-to-model comparison is made using TCs at same intensity because the TC's structure depends on the TC's intensity. This requires that we predetermine the intensity values at which the model-to-model comparison is made. In this study, such intensity values are set using  $\text{WS}_{\max}$ , and we use the term "stage" to indicate the intensity of TCs (Table 1). For example, stage 7 corresponds to  $\text{WS}_{\max}$  between 24 and  $27 \text{ m s}^{-1}$ .

We first azimuthally average select fields around the TC centers; hereafter, a "snapshot" indicates an azimuthally averaged field. Individual snapshots are then classified into their corresponding stages. The averages of each stage yield the TC composite fields. Snapshots of TCs poleward of  $25^{\circ}\text{N}$  and  $25^{\circ}\text{S}$  are excluded so as to focus on the structures of TCs in the deep tropics. We also excluded snapshots during the decaying phase of TCs' life cycles (i.e., after the lifetime minimum  $\text{SLP}_{\min}$ ) because our focus is on TC intensification.

Tangential, radial, and pressure velocity are used to examine the TC kinematic structures, while warm-core temperature and relative humidity are used to investigate TC thermodynamic structures. The warm-core temperature is defined here as the temperature deviation from the environmental value, defined by averaging the temperature over a 2000-km square centered at the TC but excluding the inner 1000-km square area. The moisture-convection coupling within the TCs is analyzed using precipitation, precipitable water, and free-tropospheric (850–100 hPa) column relative humidity (CRH). Surface turbulent fluxes and surface and TOA radiative fluxes are employed to examine the surface enthalpy flux feedback and the cloud-radiation feedback processes.

TABLE 1. Statistics of snapshots used in the composite analysis

Stage	Wind speed ( $\text{m s}^{-1}$ )	Probability of occurrence (%)		
		AM2.5	FLOR	HiRAM
1	6–9	0.12	0.12	0.08
2	9–12	4.32	3.79	5.20
3	12–15	12.53	12.59	16.65
4	15–18	19.44	17.69	18.81
5	18–21	20.43	21.66	17.33
6	21–24	18.38	19.74	12.56
7	24–27	12.41	12.59	9.66
8	27–30	6.67	6.65	6.22
9	30–33	3.68	3.20	4.56
10	33–35	1.36	1.33	2.90
11	35–38	0.30	0.52	2.45
12	38–41	0.24	0.07	1.78
13	41–44	0.03	0.02	1.17
14	44–47	0.09	0.00	0.53
15	47–50	0.00	0.00	0.10
No. of snapshots		3313	4058	4938
No. of TCs		152	191	247

### d. Composite on precipitation percentiles

To provide further insights among models in their TC simulations, we composite various fields onto precipitation percentiles. This composite method has been used to reveal essential characteristics of the interaction among convection, moisture, and circulation, with a particular focus on the simulation of the Madden-Julian oscillation (Kim et al. 2014). Precipitation percentiles represent the models' own regimes of strong, moderate, and weak convection, and compositing various fields on precipitation percentiles allows us to assess natural characteristics of each model's precipitation distribution and its relationship to other variables of interest. We use grid points located over the oceans between  $5^{\circ}$  and  $25^{\circ}\text{N}$  and between  $5^{\circ}$  and  $25^{\circ}\text{S}$  around the peak of tropical cyclone seasons (i.e., July–September for the Northern Hemisphere and January–March for the Southern Hemisphere) in 1984 and 1985. Grid points that are within 1000 km from the TC's center are excluded to remove the effects of TCs. Six-hourly rain rates are used to define the precipitation percentile bins, and various fields are averaged for each bin. The averaged fields are shown as a function of precipitation percentiles (e.g., Fig. 12). To facilitate the comparison with TC composite results, the percentiles are shown descending from left to right.

## 3. Results

### a. TC intensity

Figure 1 shows the time series of  $\text{SLP}_{\min}$  and  $\text{WS}_{\max}$  of all TCs used in the TC composite analysis. These two

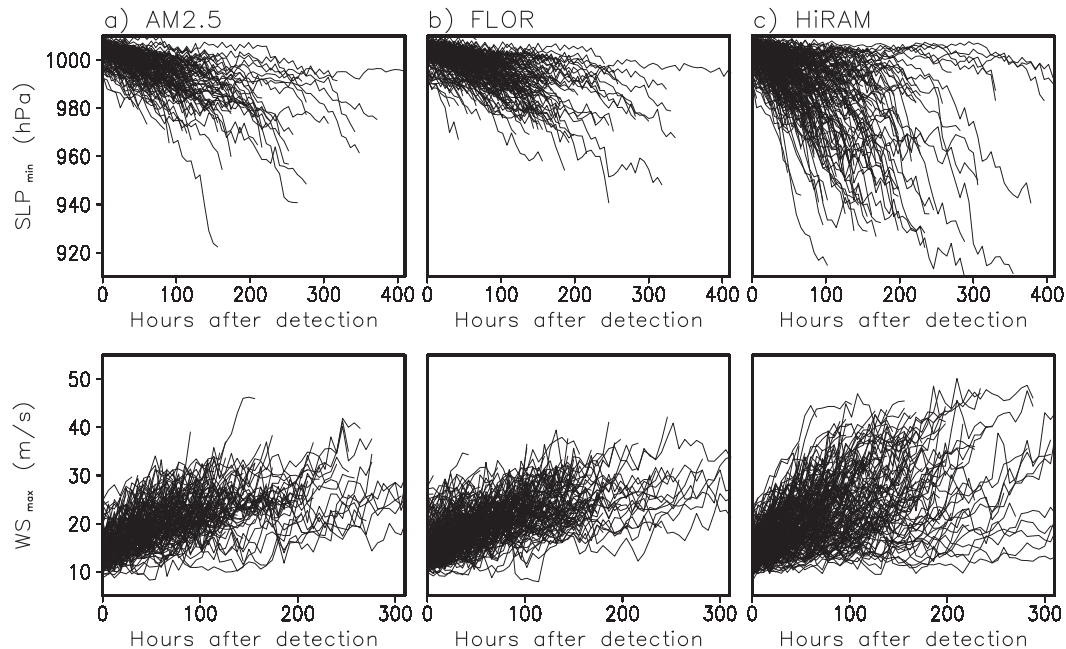


FIG. 1. Time evolution of (top) minimum SLP ( $SLP_{\min}$ ) and (bottom) maximum surface wind speed ( $WS_{\max}$ ) of TCs detected in (a) AM2.5, (b) FLOR, and (c) HiRAM simulations.

variables are commonly used to estimate TC intensity, and the  $SLP_{\min}$ – $WS_{\max}$  relationship has been extensively explored in the literature (e.g., Dvorak 1975; Atkinson and Holliday 1977; Holland 1980, 2008; Knaff and Zehr 2007; Kossin 2015). AM2.5 and FLOR exhibit similar features, while HiRAM produces, in general, notably stronger TCs in terms of both  $SLP_{\min}$  and  $WS_{\max}$ . The exception is one event in AM2.5 that develops with  $SLP_{\min}$  lower than 930 hPa and  $WS_{\max}$  greater than  $45 \text{ m s}^{-1}$ . Figure 2 shows scatterplots of  $SLP_{\min}$  and  $WS_{\max}$  for TCs detected in the simulations. The relationship between  $SLP_{\min}$  and  $WS_{\max}$  could be affected by model configurations, such as those that affect surface friction or vertical momentum mixing. Blue and red lines show the least squared power function fits of the best-track data from Atkinson and Holliday (1977) and Knaff and Zehr (2007), respectively. The least squared power function fits to the model simulation results follow those derived from observations for relatively weak TCs and start to deviate from the observation best-fit line as the intensity of TCs increases.  $WS_{\max}$  is comparable across all models for  $SLP_{\min}$  between 970 and 990 hPa, and  $WS_{\max}$  increases more slowly with  $SLP_{\min}$  decrease in AM2.5 and FLOR than in HiRAM. Note that other 50-km mesh GCMs have shown a  $SLP_{\min}$ – $WS_{\max}$  relationship that is similar to HiRAM's (e.g., Manganello et al. 2012; Roberts et al. 2015).

It is apparent from Figs. 1 and 2 that HiRAM simulates stronger TCs than AM2.5 and FLOR. Only HiRAM

produces a sizable number of TC snapshots with  $SLP_{\min} < 960 \text{ hPa}$  or with  $WS_{\max} > 30 \text{ m s}^{-1}$ . The frequency distribution of the number of snapshots in each stage (Table 1) also shows that over 10% of snapshots are associated with  $WS_{\max} > 30 \text{ m s}^{-1}$  in HiRAM. This percentage drops to 5.7% and 5.1% in AM2.5 and FLOR, respectively, suggesting that the HiRAM model tends to develop more intense TCs than the other models. The above results set our central question: Why does HiRAM simulate stronger TCs than the other models? Although the individual GFDL models that we use have been actively used to study TCs (e.g., Zhao et al. 2012; Vecchi et al. 2014), little attention has been paid to intermodel comparisons among those GFDL GCMs.

#### b. Large-scale environmental fields

First, we examine a few of the large-scale environmental parameters to determine if they can explain the differences of TC intensity between HiRAM and the other models. Earlier studies have shown that TC intensity is affected by large-scale parameters such as vertical wind shear, PI, and lower- and middle-tropospheric humidity (e.g., Emanuel 1988; DeMaria and Kaplan 1994; Kaplan and DeMaria 2003; DeMaria et al. 2005). Although the same observed SSTs are prescribed as the boundary condition in both AM2.5 and HiRAM, they could simulate different background environmental states. In FLOR, this possibility is even greater, as it predicts SST, although the

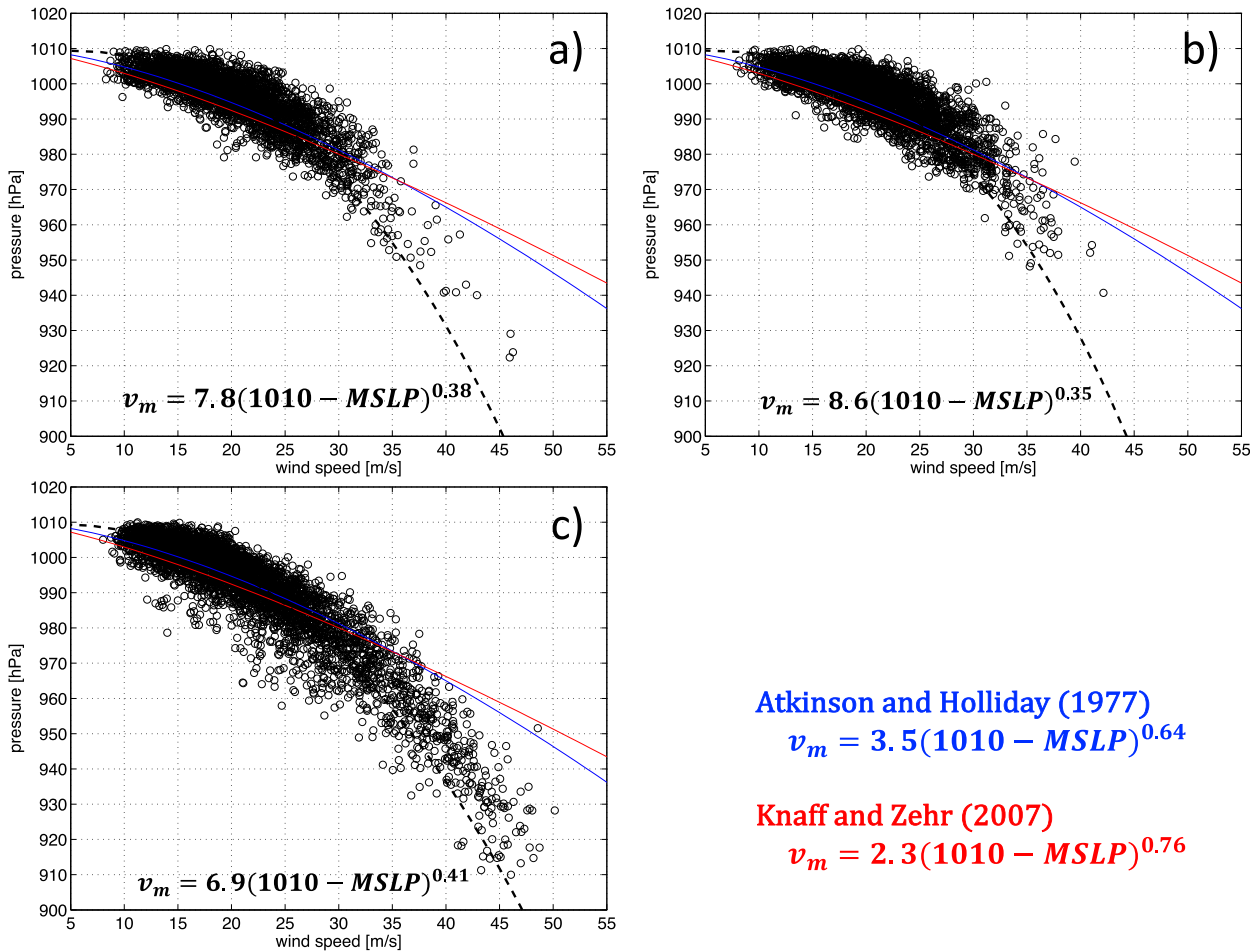


FIG. 2. Scatterplots of minimum SLP vs maximum surface wind speed for TCs detected in (a) AM2.5, (b) FLOR, and (c) HiRAM simulations. Blue and red lines show the least squared power function fits of the best-track data from Atkinson and Holliday (1977) and Knaff and Zehr (2007), respectively. Black dashed lines show the least squared power function fits applied to the simulations. The regression equations for the fits are shown in the bottom of the panels.

SST difference is small, as the SST is nudged toward observations (not shown).

None of the large-scale parameters tested—environmental vertical wind shear (between 850 and 200 hPa), 600-hPa relative humidity, and PI—can explain the occurrence of stronger TCs in HiRAM. Figure 3 shows the PI<sup>1</sup> as an example of the differences in environment among the models. The PI was calculated here using the formulation of Bister and Emanuel (2002). The PI is commonly used to explain simulated changes in TC intensity in future climates (e.g., Vecchi and Soden

2007; Held and Zhao 2011; Camargo 2013; Wehner et al. 2015; Ting et al. 2015; Sobel et al. 2016). In each hemisphere, an average over peak TC season (August–October for Northern Hemisphere and January–March for Southern Hemisphere) is shown. Figure 3 shows that PI in HiRAM is not substantially higher than that in the other models (if anything, it is lower). Over the Northern Hemisphere’s western Pacific warm pool region, for example, AM2.5 and FLOR show higher PI values than HiRAM. We conclude that the PI alone is unable to explain why HiRAM simulates stronger TCs than the other models. Similar results are obtained with vertical wind shear and 600-hPa relative humidity (not shown). Therefore, our results suggest that in this ensemble of three models, differences in large-scale environmental parameters do not offer an adequate explanation for the intermodel differences in simulated TC activity, consistent with earlier single-model (e.g., Reed et al. 2015)

<sup>1</sup> To aid future comparisons with our results, we provide here the parameters and the assumptions used in the calculation of the PI: exchange coefficient rates ( $C_k/C_d$ ) = 0.9; surface reduction = 0.8; exponent reduction for azimuthal velocity in the eye = 2; reversible ascent is assumed; and dissipative heating is allowed.

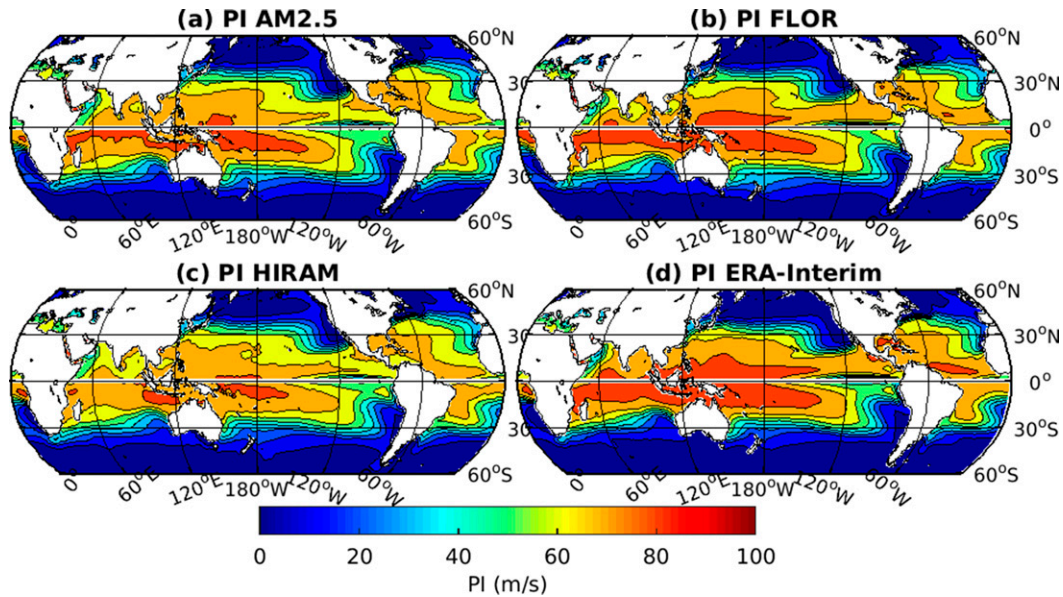


FIG. 3. The PI ( $\text{m s}^{-1}$ ) in (a) AM2.5, (b) FLOR, (c) HiRAM, and (d) ERA-Interim. Average over peak TC season is shown in each hemisphere (August–October for NH and January–March for SH).

and multimodel comparison papers (e.g., Camargo et al. 2007; Camargo 2013).

### c. Tropical cyclone structures

In this subsection, we compare TC structures in the three simulations with the goal of finding features that distinguish the HiRAM, with its more intense TCs, from the other two models. We first focus on the dynamical structures of the simulated TCs and then analyze features that have close connections to moist physics. The focus of our discussion will be on the differences between AM2.5 and HiRAM for two reasons: (i) the TC intensity distribution is similar in AM2.5 and FLOR, and (ii) the comparison between AM2.5 and HiRAM will isolate the role of moist physics, the only difference between the two models. However, we should emphasize that the similarity of the TC intensity distributions in AM2.5 and FLOR is an important result, showing that using fixed SST or coupling the atmospheric model to the ocean does not lead to fundamental differences in TC intensity distribution in this model. This is also consistent with the findings of Murakami et al. (2015); a relatively short, 5-day time scale for SST nudging in the FLOR simulation might have minimized the effect of air–sea interaction on TC intensity.

Figures 4–6 compare azimuthally averaged kinematic and thermodynamic structures of TCs at selected stages (4, 7, and 10, which correspond to 15–18, 24–27, and 33–36  $\text{m s}^{-1}$   $WS_{\max}$  intervals, respectively). Overall, the

50-km-resolution GCMs show structures that are qualitatively similar to the structure of observed TCs. The composite structures show a cyclonic circulation around the TC center, with a low-level radial inflow toward the center and a layer of radial outflow near 200-hPa level below the tropopause (Fig. 4). Near the center, all models exhibit a pronounced positive warm-core temperature anomaly (Fig. 5) and strong upward motion with nearly saturated low-tropospheric conditions (Fig. 6). At stage 10, with  $WS_{\max}$  between 33 and 36  $\text{m s}^{-1}$ , the warm-core temperature anomalies reach about 8 K in AM2.5 and 10 K in HiRAM at around 300 hPa (Fig. 5).

Notable discrepancies exist between modeled and observed TC structures. For example, the models show the maximum tangential wind near 900 hPa at around 100–150 km from the center (Fig. 4), while in observations, the radius of maximum wind (RMW) is typically 50 km or less from the TC center (e.g., Kimball and Mulekar 2004). Unlike observed TCs that exhibit the strongest upward motions within the eyewall and subsidence in the eye, the modeled TCs show upward motions at the center without an eyelike feature. The precipitation and precipitable water composite fields also demonstrate the absence of an eye (Fig. 7). Examination of all detected TCs reveal that most TCs lack an eyelike feature, except those that reach an extremely high intensity (Fig. 8). The larger-than-observed size of TCs and the lack of an eyelike feature in the low-resolution GCMs have been extensively discussed in the literature (e.g., Bengtsson et al. 1995; Vitart et al.

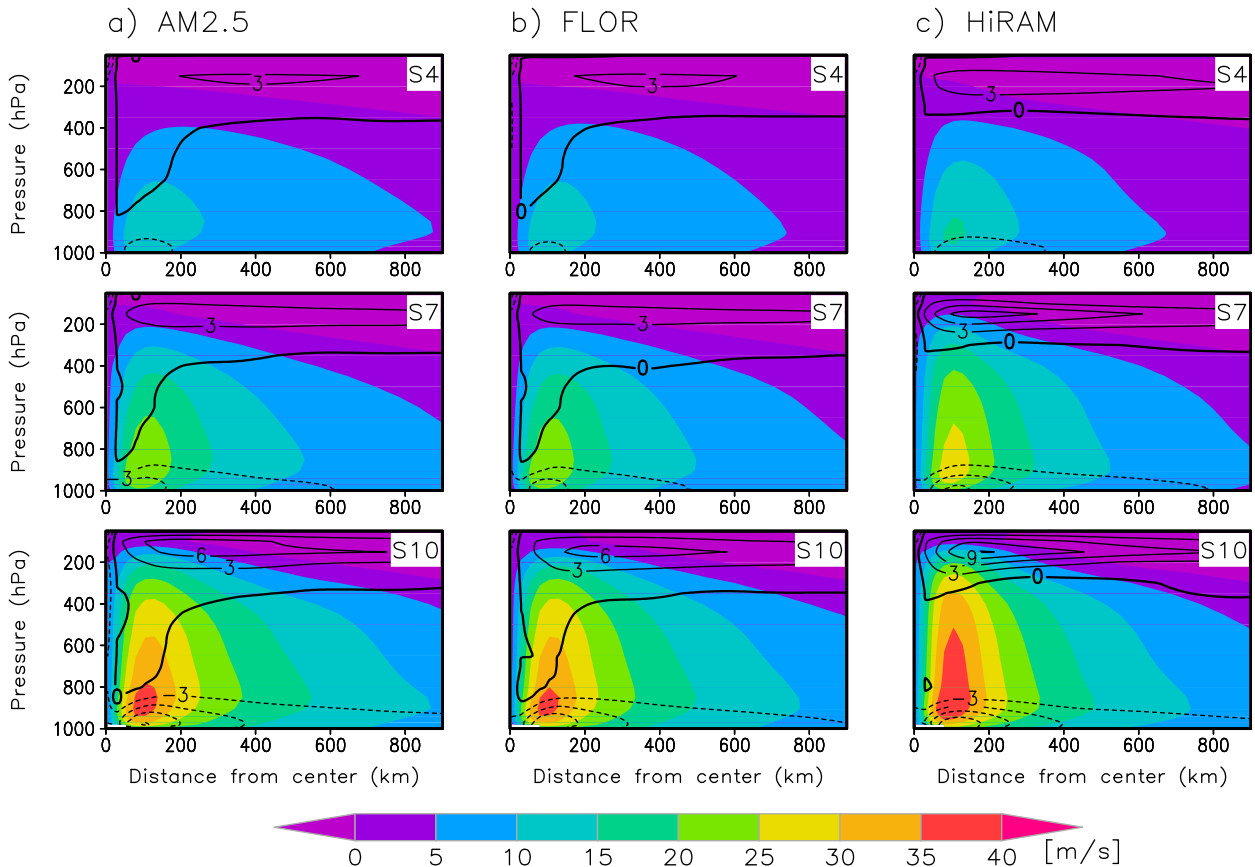


FIG. 4. Structure of TCs in (a) AM2.5, (b) FLOR, and (c) HiRAM simulations. Tangential ( $\text{m s}^{-1}$ , color shaded) and radial velocity ( $\text{m s}^{-1}$ , contours) are composited azimuthally around TC centers for stages (top) 4, (middle) 7, and (bottom) 10. Contour interval is  $3 \text{ m s}^{-1}$ . Solid and dashed contours indicate positive and negative values, respectively.

1997; Camargo et al. 2005), as well as how these issues improve with model resolution (e.g., Bengtsson et al. 2007; Manganello et al. 2012; Roberts et al. 2015).

In spite of the fact that the gross features of TC structures are qualitatively similar among the models, there are noteworthy differences that might provide insights into the intensity differences identified in section 3a. The vertical structure of vertical motion near the TC center exhibits a marked difference between the models (Fig. 6). HiRAM shows a top-heavy structure with a maximum vertical velocity at about 300 hPa, while the other two models exhibit a maximum vertical velocity at about 800 hPa. The magnitude of maximum vertical velocity is also greater in HiRAM than in the other two models. This difference seems to affect the vertical structure of radial wind and the warm-core temperature anomalies, especially near the center. The radial wind composites show that TCs in HiRAM exhibit radial inflows that span from the surface to the upper troposphere with a thin layer of radial outflow above 300 hPa, while AM2.5 and FLOR show an inflow

below 850 hPa and a vertically thick radial outflow layer above (Fig. 4). HiRAM also shows a more top-heavy structure of the warm-core temperature anomalies (Fig. 5) than the other two models.

Another noteworthy difference between HiRAM and the other models is that TCs are associated with stronger secondary circulations in HiRAM in composites that correspond to the same  $WS_{\text{max}}$  range (i.e., the same stage). For example, while the AM2.5 upper-level radial outflow barely reaches  $6 \text{ m s}^{-1}$  in stage 7, the magnitude of the HiRAM radial outflow exceeds  $9 \text{ m s}^{-1}$  (Fig. 4). The maximum warm-core temperature anomaly in HiRAM is also 2–3 K greater than that in AM2.5 (Fig. 5). At a given stage, the vertical velocity is also stronger in HiRAM throughout the troposphere, particularly in the upper troposphere (Fig. 6). We will show below that HiRAM produces more precipitation near the TC's center at a given stage. With stronger vertical velocity and upper-level radial outflow near the center, the relative humidity at the upper troposphere is much higher and widespread around the center in HiRAM. The radial



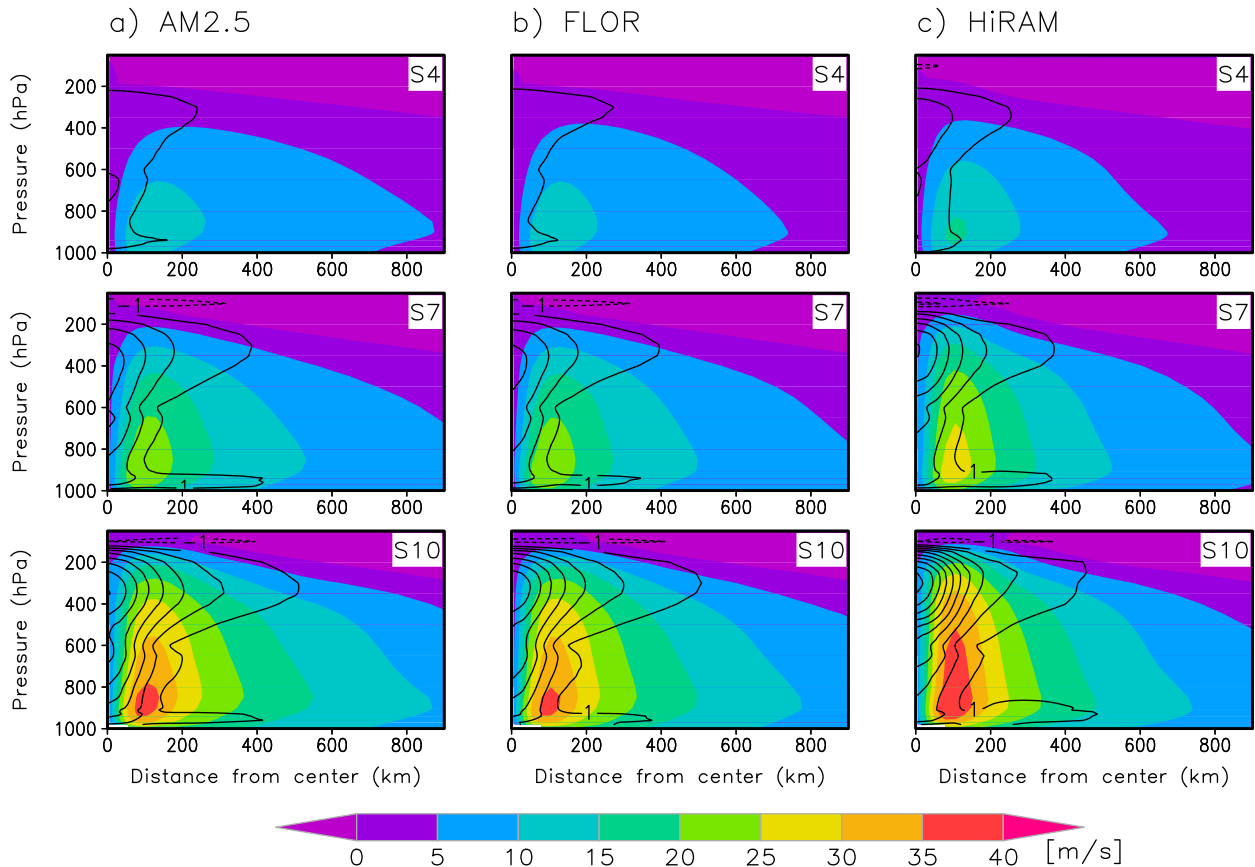


FIG. 5. As in Fig. 4, but for tangential velocity ( $\text{m s}^{-1}$ , color shaded) and warm-core temperature (K, contours). The warm-core temperature is a temperature anomaly from average over a 500–1000-km range around the TC center. The contour interval is 1 K, and the zero line is omitted. Solid and dashed contours indicate positive and negative values, respectively.

gradient of relative humidity in the midtroposphere (400–600 hPa) is also much larger in HiRAM than in the other models, especially closer to the center (between  $r = 200$  and 600 km) and for weaker storms.

Figure 7 shows distributions of precipitation rate, precipitable water, and CRH around the TCs. There is a striking difference in the precipitation field within 200 km from the TC center between HiRAM and the other models (Fig. 7a). For a given stage, the HiRAM model produces more precipitation—thus, more column-integrated diabatic heating—near the center. For example, in stage 7, the mean precipitation produced by HiRAM near the center is about  $13 \text{ mm h}^{-1}$ , which is approximately 44% greater than that of the other models ( $\sim 9 \text{ mm h}^{-1}$ ). A greater amount of diabatic heating near the center would provide favorable conditions for further TC development and intensification. This is because the efficiency in converting the injected heat energy to the kinetic energy of the TC's swirling circulation is greater closer to the center, where inertial stability is higher (e.g., Schubert and Hack 1982; Shapiro and Willoughby 1982;

Hack and Schubert 1986; Nolan et al. 2007). Therefore, our results suggest that the greater amount of diabatic heating near the center would allow TCs to have higher chances of further intensification in HiRAM than in AM2.5 and FLOR. Consequently, the next question is this: Why does the HiRAM model produce more rain near the center than the other models?

The precipitable water near the TC's center exhibits similar values across all models regardless of the stage considered (Fig. 7b), ruling out the possibility that HiRAM produces more rainfall because it has more water vapor in the column close to the TC centers. On the other hand, there are notable differences in CRH (Fig. 7c). When TCs become more intense (stage  $> 7$ ), a local minimum in CRH appears at the TC centers in AM2.5 and FLOR, while for HiRAM, the local minimum is absent (stage 7) or is much less pronounced (stage 10). In the relative humidity composite for stage 10, these two models show values lower than 90% throughout most of the free troposphere (above 800 hPa) near the center (Fig. 6), indicating that AM2.5

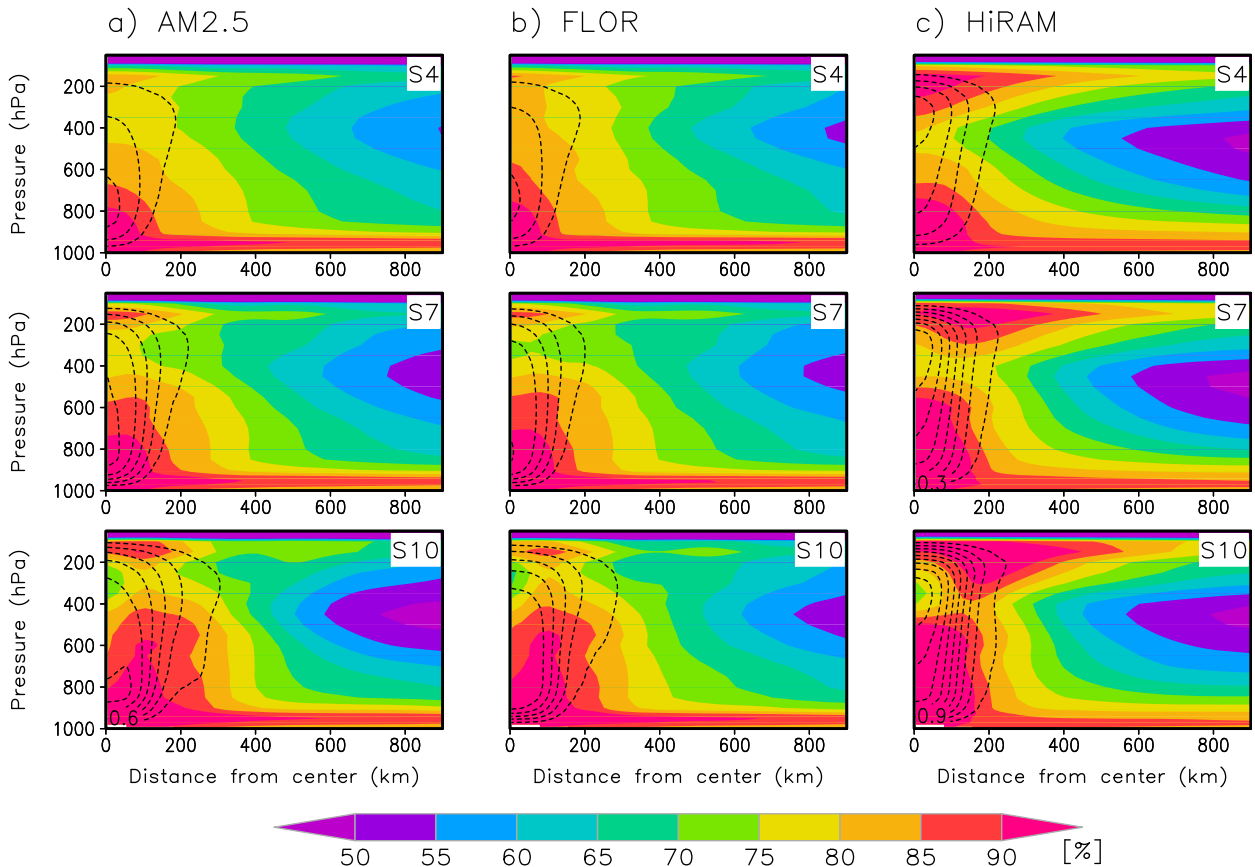


FIG. 6. As in Fig. 4, but for relative humidity (%), color shaded, and pressure velocity ( $\text{Pa s}^{-1}$ , contours). Contour interval is  $0.3 \text{ Pa s}^{-1}$ , and the zero line is omitted. Solid and dashed contours indicate positive and negative values, respectively.

and FLOR tend to develop a relatively dry region at the core of intense TCs. In HiRAM, in contrast, air with relative humidity lower than 90% appears over a much shallower layer between 500 and 200 hPa (Fig. 6), and only a slightly lower local minimum is found in CRH (Fig. 7). As a result, the contrast in CRH between inner-core (e.g., 100 km from the center) and outer-core parts (e.g., 600 km from the center) of TCs is larger in HiRAM than in the other models.

To gain further insight into the precipitation distribution near the TC's center, the relationships of precipitation rate with precipitable water and CRH are presented in Fig. 9. Composites of the fields at all stages are used. All models show a tight coupling between precipitable water and precipitation rate; precipitation rate increases exponentially with precipitable water when precipitable water is greater than approximately 55 mm (Fig. 9a). Figure 9a also shows that the rate at which precipitation increases with precipitable water is larger in HiRAM than in the other models. Furthermore, while the precipitation rate seems to reach its maximum ( $\sim 15 \text{ mm h}^{-1}$ ) at a precipitable water value of

about 72 mm and shows no further increase in AM2.5 and FLOR, HiRAM continues to increase until the precipitation rate is approximately  $20 \text{ mm h}^{-1}$  at a precipitable water value of about 75 mm. As a result, for precipitable water greater than 70 mm, HiRAM produces more precipitation than the other two models.

HiRAM also shows a much tighter CRH–precipitation relationship (Fig. 9b). For CRH about 0.87, precipitation in AM2.5 and FLOR spans from about 2 to about  $15 \text{ mm h}^{-1}$ , while the range is much narrower in HiRAM ( $4\text{--}6 \text{ mm h}^{-1}$ ). Furthermore, for precipitation rates greater than  $9 \text{ mm h}^{-1}$ , the relationship between the two variables in HiRAM is markedly different from the other two models; precipitation increases monotonically with CRH up to CRH value 0.95 in HiRAM, while the monotonic increase stops at a CRH value of about 0.9 in AM2.5 and FLOR. This seems to be related to the fact that CRH shows a pronounced local minimum at TC centers in AM2.5 and FLOR (Fig. 7), which prevents AM2.5 and FLOR from having CRH greater than 0.9. HiRAM also exhibits a weak signal of precipitation saturation in the regime of

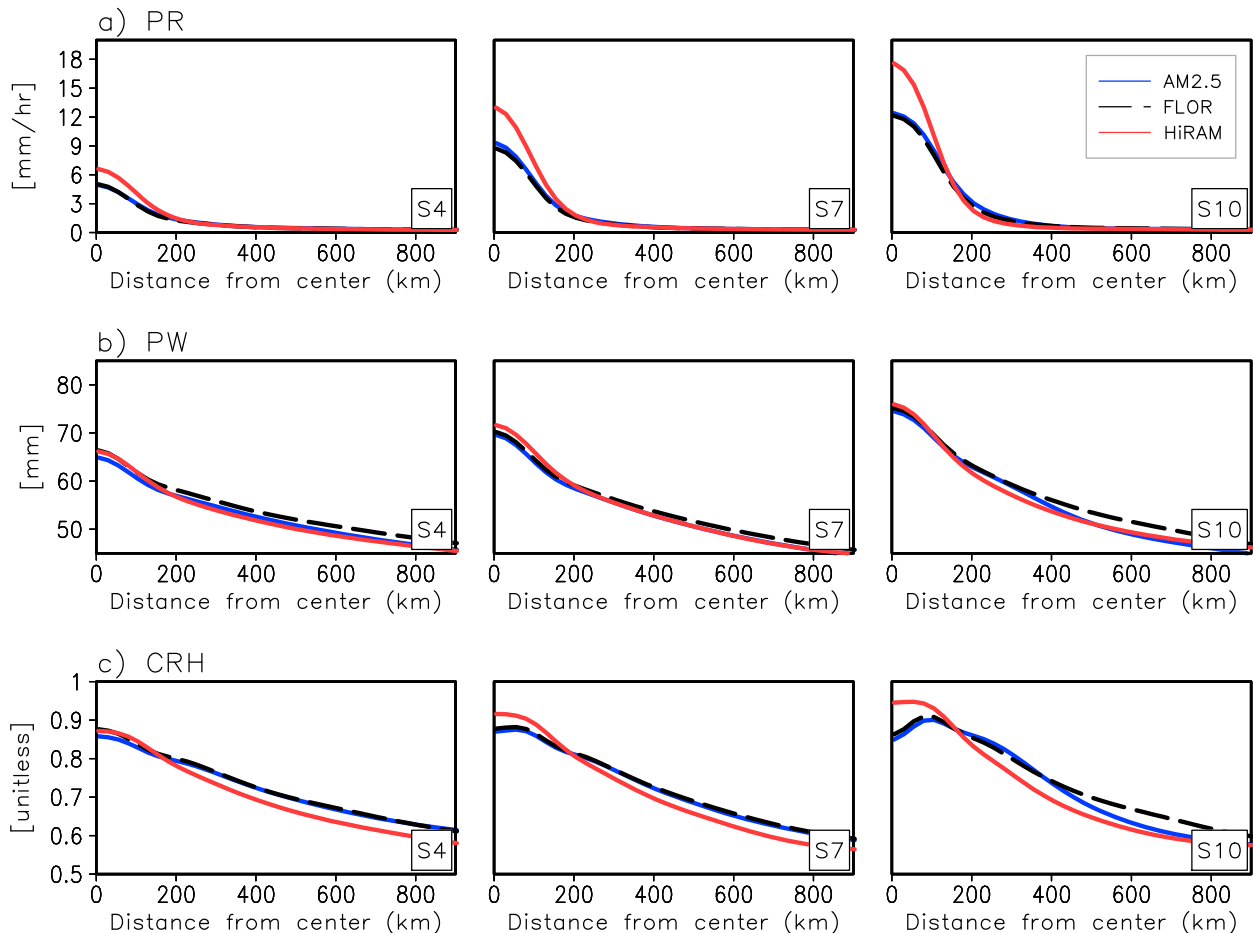


FIG. 7. Structure of TCs in AM2.5 (blue), FLOR (black), and HiRAM (red) simulations. (a) Precipitation ( $\text{mm h}^{-1}$ ), (b) precipitable water (mm), and (c) free-tropospheric column relative humidity (no unit) are composited azimuthally around TC centers for stages (left) 4, (center) 7, and (right) 10. The free-tropospheric column relative humidity is the ratio of vertically integrated specific humidity to vertical integral of saturation specific humidity over the free troposphere (850–100 hPa).

very high precipitation ( $>20 \text{ mm h}^{-1}$ ), where CRH is around 0.95.

Figure 10 compares the net vertical moist enthalpy flux convergence near TC centers for all models. The surface turbulent and radiative fluxes and top-of-atmosphere (TOA) radiative fluxes are used to obtain the net moist enthalpy flux convergence, that is, the difference between net flux at the surface and TOA. Our results show that the net flux convergence is greater in HiRAM than in the other models near the TC center, especially for stronger storms (Fig. 10). The difference between HiRAM and the other models is larger than  $100 \text{ W m}^{-2}$  within 100 km from the center at stage 10, indicating that significantly more energy goes into the column near the center in HiRAM than in the other models. HiRAM also shows a larger difference in net moist enthalpy flux convergence between the inner core and surrounding regions of TCs throughout the stages.

The surface latent heat flux is the major contributor to the difference across the models in their net vertical moist enthalpy flux convergence (Fig. 10b). The bulk aerodynamic formula of the surface latent heat flux suggests that the flux is proportional to the near-surface wind speed and air–sea humidity difference. At stage 7, HiRAM simulates a greater near-surface wind speed and air–sea humidity difference in the inner part ( $<200 \text{ km}$  from center) of the TCs (Figs. 10d,e), which leads the model to have a higher surface latent heat flux (Fig. 10b). Note that we use winds at the lowermost model level to approximate near-surface winds in Fig. 10.

Outgoing longwave radiation (OLR) plays the second largest role in the intermodel difference in the net vertical moist enthalpy flux convergence. The reduction in the magnitude of OLR (i.e., less emission of longwave radiation to space) by anomalous moisture and clouds

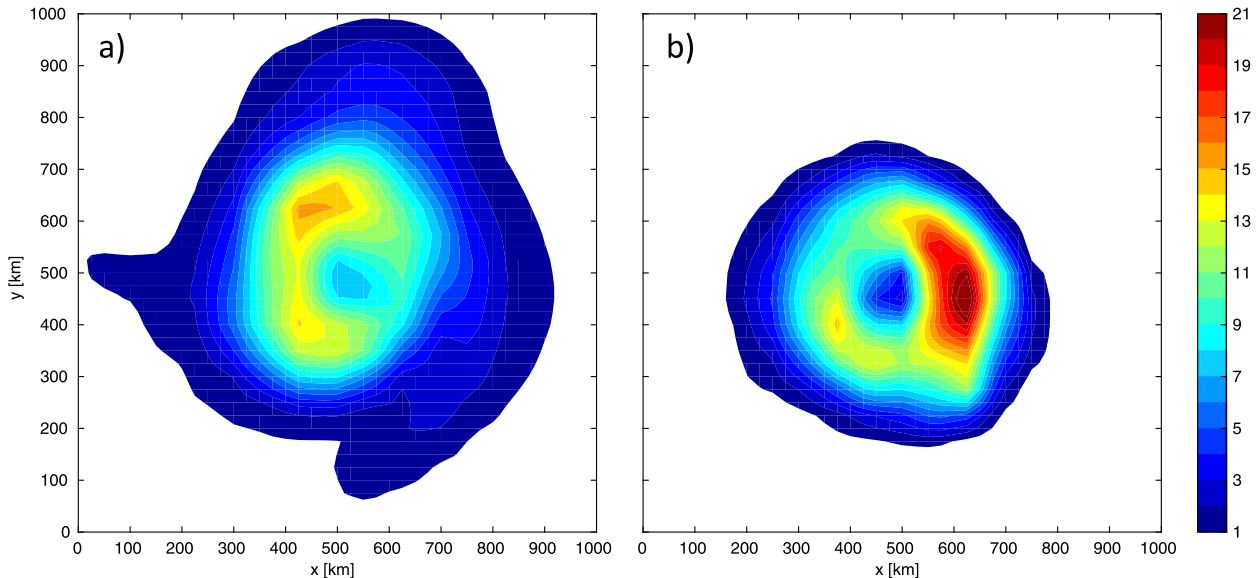


FIG. 8. Precipitation ( $\text{mm day}^{-1}$ ) around an intense TC simulated in (a) AM2.5 ( $\text{SLP}_{\min} = 928.5 \text{ hPa}$ ) and (b) HiRAM ( $\text{SLP}_{\min} = 928.5 \text{ hPa}$ ) simulations.

near the center relative to outer radii is larger in HiRAM than in the other models, which is consistent with the greater rain rate (Fig. 7) and higher upper-level relative humidity (Fig. 6). This longwave feedback was found to be the most important process by Camargo and Sobel (2004) in a study of TC-like vortices in a much lower-resolution model; those much weaker vortices, unlike those in HiRAM, could not generate winds strong enough to produce a strong latent surface heat flux feedback.

#### d. Precipitation percentile composites

Our results suggest that the distribution of TC intensity is related to the TC structure—TCs' structures are more favorable for further intensification (more precipitation near the TC center) in HiRAM than in the

other two models, and HiRAM simulates intense TCs more frequently than the other two models do. In this subsection, we aim to understand the intermodel differences in TC structure using composites based on precipitation percentiles. As mentioned in section 2c, precipitation percentile composites can be used to examine how convection interacts with other fields, such as moisture and surface heat flux. While the precipitation percentile composites reveal general characteristics of the model, especially its moist physics, the diagnostics are not specific to TCs, as we exclude the area around TC centers from the compositing. Therefore, comparisons between precipitation percentiles and TC composites would reveal the degree to which the TC structure is affected by the parameterization characteristics.

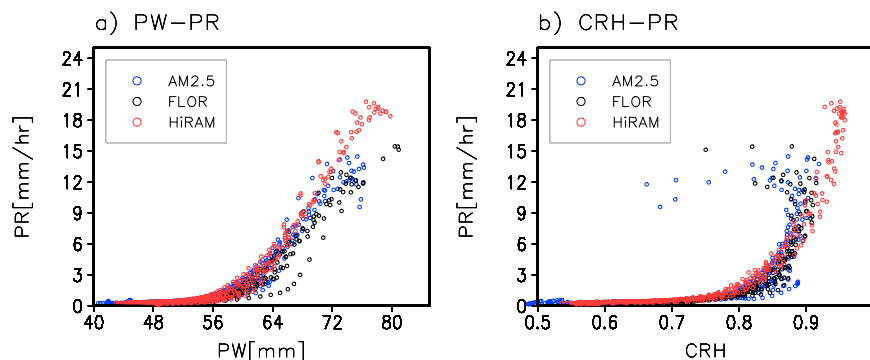


FIG. 9. Scatterplot between (a) precipitable water vs precipitation and (b) free-tropospheric column relative humidity vs precipitation. The composited values for all stages are used. Blue, black, and red circles indicate AM2.5, FLOR, and HiRAM, respectively.

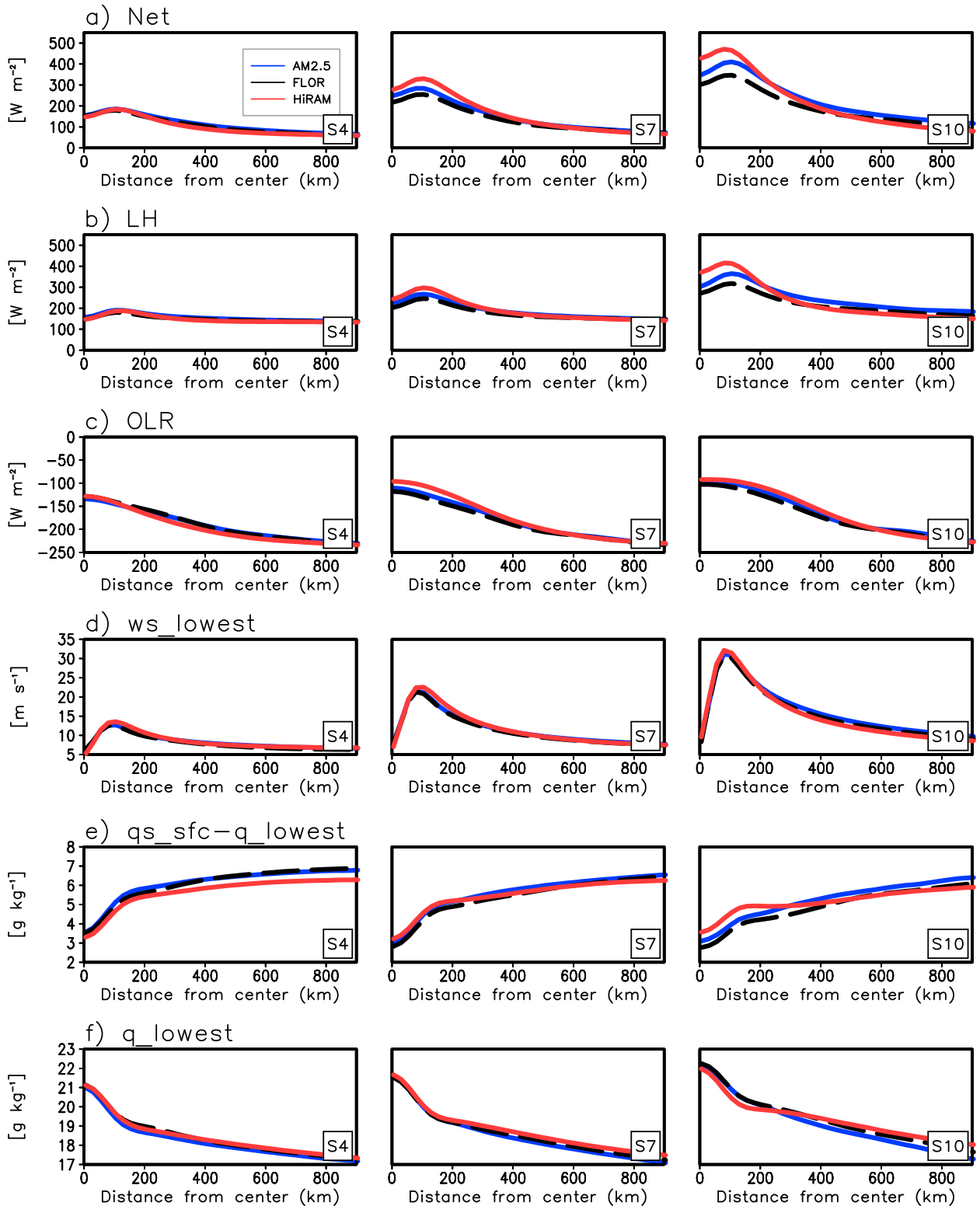


FIG. 10. As in Fig. 7, but for (a) net total enthalpy flux into the column from surface and TOA ( $\text{W m}^{-2}$ ), (b) surface latent heat flux ( $\text{W m}^{-2}$ ), (c) outgoing longwave radiation ( $\text{W m}^{-2}$ ), (d) near-surface wind speed ( $\text{m s}^{-1}$ ), (e) air-sea humidity difference ( $\text{g kg}^{-1}$ ), and (f) near-surface specific humidity ( $\text{g kg}^{-1}$ ). Blue, black, and red curves indicate AM2.5, FLOR, and HiRAM, respectively.

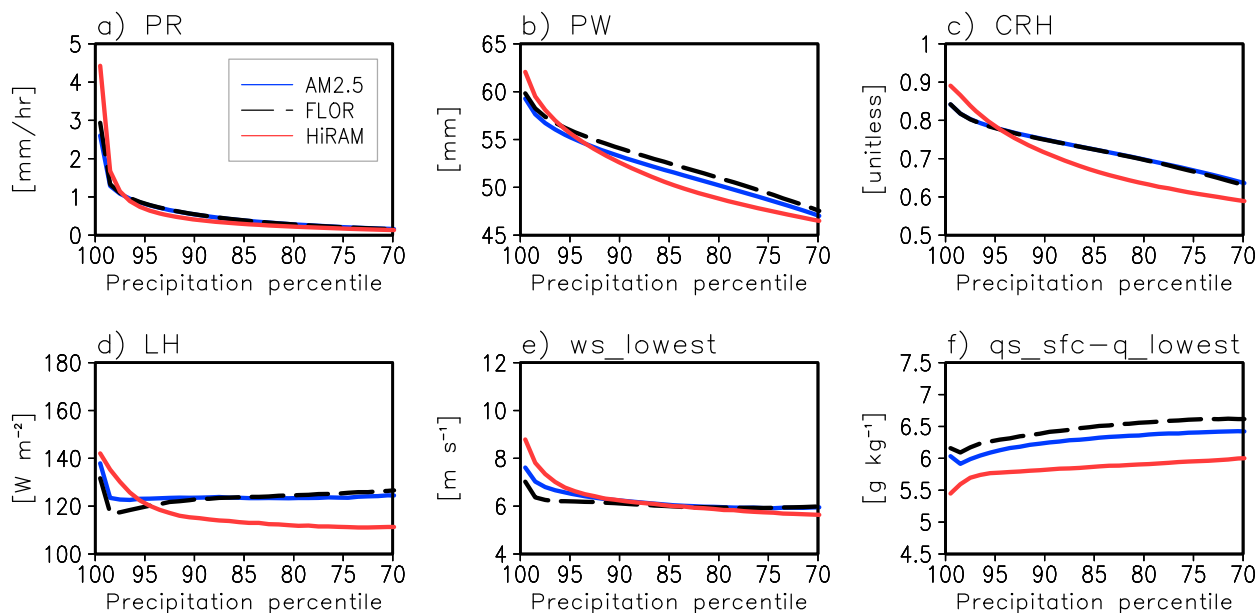


FIG. 11. (a) Precipitation ( $\text{mm h}^{-1}$ ), (b) precipitable water (mm), (c) free-tropospheric column relative humidity (no unit), (d) surface latent heat flux ( $\text{W m}^{-2}$ ), (e) near-surface wind speed ( $\text{m s}^{-1}$ ), and (f) air-sea humidity difference ( $\text{g kg}^{-1}$ ) composited on precipitation percentiles. Blue, black, and red curves indicate AM2.5, FLOR, and HiRAM, respectively.

Precipitation values corresponding to the top 30 percentiles are shown in Fig. 11a. AM2.5 and FLOR rain rates are higher than that of HiRAM, except for the top few percentiles. Note that grid points near the model TCs are excluded from this composite analysis. Precipitable water and CRH increase monotonically with the precipitation percentile in all models (Figs. 11b,c), indicating that heavier rain events occur in moister environments. What distinguishes HiRAM from the other models is the greater contrast between the strong and moderate rain-rate regimes. For example, the difference in CRH between the 99th and 70th precipitation percentiles is about 2 times larger in HiRAM than in the other models. This suggests that a transition from a moderate to strong rain-rate regime would require a greater moistening, that is, convection is more sensitive to the environmental moisture in HiRAM than in the other models.

Figure 12 shows relative humidity and pressure velocity composited on precipitation percentiles. Again, the contrast between heavy and weak rain-rate regimes is weaker in AM2.5 and FLOR than in HiRAM. The relative humidity is higher in general in HiRAM, especially for the top 10% rain-rate events and near the tropopause. These differences mimic the difference between HiRAM and the other models shown in the TC composites (Fig. 6). Figure 13 indicates that compared to AM2.5 and FLOR, HiRAM shows greater differences in relative humidity and vertical motion between strong (top 5%) and moderate (60th–80th percentiles)

rain-rate events. Again, this contrast between the models is similar to the intermodel difference shown in the TC composites (Fig. 6), suggesting that the precipitation percentile composites are useful diagnostics to infer parameterization characteristics that affect the models' typical TC structure.

Composites of surface latent heat flux, near-surface wind speed, and air-sea humidity difference are shown in Figs. 11d–f. In HiRAM, heavier precipitation events are associated with stronger surface latent heat flux, while in the other models, the surface latent heat flux tends to become weaker in the intense precipitation regime (Fig. 11d). The increase in near-surface wind speed is responsible for the increase in surface latent heat flux at the highest percentiles in HiRAM (Fig. 11e). This might suggest a strong feedback between precipitation and surface latent heat flux in HiRAM; the convection enhances the surface latent heat flux via stronger winds near the surface, and the increased surface flux further strengthens the convection. Recall that the latent heat flux, and its difference between the TC's center and its surroundings, was larger in the HiRAM TC composites (Fig. 10).

#### 4. Summary and conclusions

High-resolution GCMs have become indispensable tools for seasonal and subseasonal TC predictions and future projections of TC activity. Previous studies have shown that TC intensity in GCMs is sensitive to details

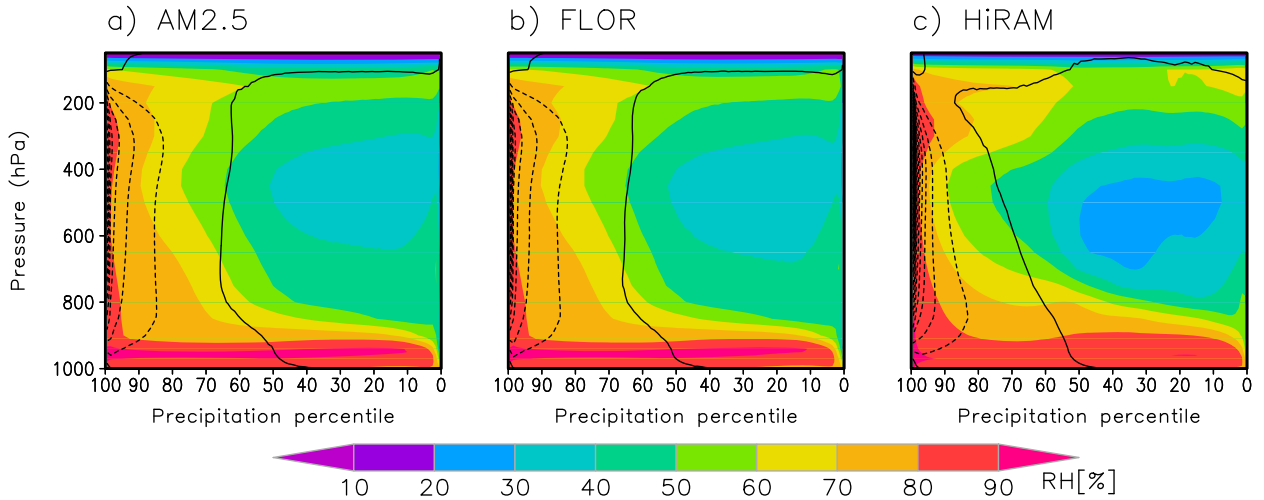


FIG. 12. Relative humidity (% , color shaded) and pressure velocity ( $\text{Pa s}^{-1}$ , contours) composited on precipitation percentiles for (a) AM2.5, (b) FLOR, and (c) HiRAM. Contour interval is  $0.1 \text{ Pa s}^{-1}$ . Solid and dashed contours indicate positive and negative values, respectively.

of the cumulus parameterization, suggesting that the large intermodel spread in TC intensity among models is influenced by the differences in the models' convection schemes. The goal of the current study is to identify processes that determine TC intensity in GCMs. For this purpose, we developed a set of process-oriented TC intensity diagnostics that are relevant to parameterization schemes and TC dynamics.

Two 50-km-resolution GCMs in three different configurations—AM2.5, FLOR, and HiRAM—are used in this study. We analyzed two years of model simulations forced with observed SST as the boundary condition (AM2.5 and HiRAM) and coupled with an ocean model whose SSTs are nudged toward observed SSTs (FLOR).

TC-like vortices were detected and tracked in the models' outputs using standard tracking algorithms. The 2-yr period analyzed here is part of longer model simulations, and the TC statistics are typical of each model.

Compared to AM2.5 and FLOR, HiRAM tends to develop stronger TCs. The frequency distribution of  $WS_{\max}$  (Table 1) showed that the incidence of TCs with  $WS_{\max}$  greater than  $30 \text{ m s}^{-1}$  is much higher in HiRAM (13.5%) than in AM2.5 (5.7%) and FLOR (5.2%). Large-scale environmental fields such as PI are not able to explain the difference in TC intensity distribution between HiRAM and the other two models.

TC structures were examined by compositing various fields around the TC centers. Because the purpose of the

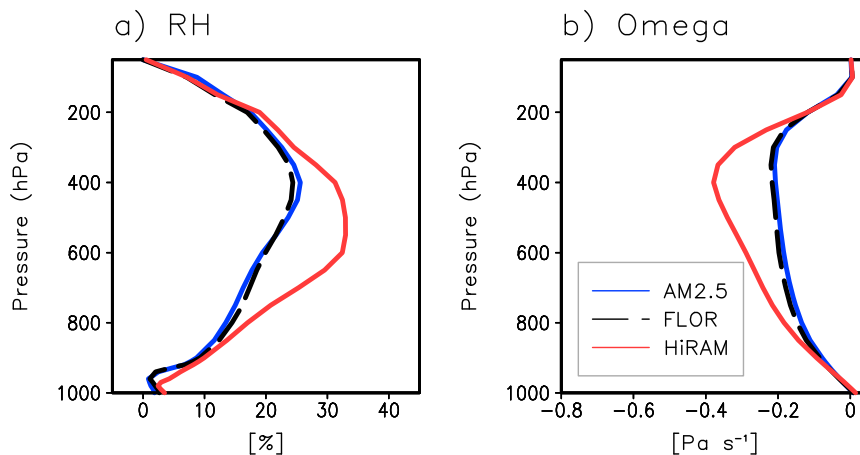


FIG. 13. Differences in (a) relative humidity (%) and (b) pressure velocity ( $\text{Pa s}^{-1}$ ) between averages for upper 5% and for 60th–80th precipitation percentiles. Blue, black, and red curves indicate AM2.5, FLOR, and HiRAM, respectively.

TC composite analysis is to understand why one of the models simulates more intense TCs than the other models, the TC composite is performed for different TC intensity bins. The 50-km-resolution GCMs show reasonable performance in capturing the overall structure of TCs, except for the larger-than-observed size of the model TCs and the absence of an eye with subsidence.

Our examination of the intermodel difference in TC structures shows that for similar TC intensity, HiRAM produces significantly more precipitation, surface latent heat flux, and column-integrated diabatic heating near the TC's center than the other models do. The greater amount of diabatic heating near the center is more favorable for TC intensification. This is consistent with studies that showed that the strength of diabatic heating and its location relative to the storm center play a critical role in determining the development of TCs (e.g., Schubert and Hack 1982; Shapiro and Willoughby 1982; Hack and Schubert 1986; Nolan et al. 2007). We show that overall, TC intensity and TC structures represented in AM2.5 and FLOR are similar. Further investigations on the role of air–sea coupling in high-resolution GCMs are required.

Precipitation percentile composites of various fields are used to assess the essential characteristics of the interaction among convection, circulation, and surface heat flux. The results show that HiRAM shows greater moisture sensitivity and a greater surface heat flux feedback through the low-level wind speed. The fact that the intermodel differences in the non-TC precipitation percentile composites (Figs. 11, 12) resemble those in the TC structures (Figs. 6, 7) demonstrates that the precipitation percentile composites are useful diagnostics to capture the natural characteristics of convection and its interaction with other fields.

Our results suggest that the moisture–convection coupling is a critical process that influences TC intensity and structure. We showed that the coupling between tropospheric moisture and convection is different among the models and that the coupling is stronger in HiRAM. This coupling is a result of feedbacks among moisture, convection, and large-scale vertical motion. The tighter moisture–precipitation relationship in HiRAM also suggests that convection is more sensitive to environmental humidity in HiRAM than in AM2.5 and FLOR. The greater moisture sensitivity of convection is likely originating from the difference in the convection scheme between HiRAM (based on a shallow convection scheme) and the other two models (relaxed Arakawa–Schubert deep convection scheme).

The process-oriented diagnostics proposed in this study may help the development of high-resolution GCMs by providing insights into the direction to

which the parameterization should be changed for a better representation of TCs. Our results warrant future studies of identifying the relationship between specific parameterization changes and the diagnostic results and of constructing the diagnostics using observations and reanalysis products.

*Acknowledgments.* This work is a contribution to the process-oriented diagnostics effort of the NOAA MAPP Model Diagnostics Task Force. We thank the Task Force members for their valuable comments during the course of this work. This study was supported by NOAA's Climate Program Office's Modeling, Analysis, Predictions, and Projections program through Grant NA15OAR4310087. D. Kim was also supported by the Korea Meteorological Administration Research and Development Program under Grant KMIPA 2016-6010 and by a startup grant from the University of Washington. Y. Moon was supported from a NSF AGS Postdoctoral Research Fellowship (AGS-1524270). The authors also thank Dr. Kun Gao (GFDL) for his constructive comments on an earlier version of the manuscript. Comments from anonymous reviewers have greatly helped the authors to improve the manuscript.

#### REFERENCES

- Atkinson, G. D., and C. R. Holliday, 1977: Tropical cyclone minimum sea level pressure/maximum sustained wind relationship for the western North Pacific. *Mon. Wea. Rev.*, **105**, 421–427, [https://doi.org/10.1175/1520-0493\(1977\)105<0421:TCMSLP>2.0.CO;2](https://doi.org/10.1175/1520-0493(1977)105<0421:TCMSLP>2.0.CO;2).
- Bacmeister, J. T., K. A. Reed, C. Hannay, P. Lawrence, S. Bates, J. E. Truesdale, N. Rosenbloom, and M. Levy, 2018: Projected changes in tropical cyclone activity under future warming scenarios using a high-resolution climate model. *Climatic Change*, <https://doi.org/10.1007/s10584-016-1750-x>, in press.
- Bengtsson, L., M. Botzet, and M. Esch, 1995: Hurricane-type vortices in a general circulation model. *Tellus*, **47A**, 175–196, <https://doi.org/10.3402/tellusa.v47i2.11500>.
- , —, and —, 1996: Will greenhouse gas-induced warming over the next 50 years lead to higher frequency and greater intensity of hurricanes? *Tellus*, **48A**, 57–73, <https://doi.org/10.3402/tellusa.v48i1.11632>.
- , K. I. Hodges, and M. Esch, 2007: Tropical cyclones in a T159 resolution global climate model: Comparison with observations and re-analyses. *Tellus*, **59A**, 396–416, <https://doi.org/10.1111/j.1600-0870.2007.00236.x>.
- Bister, M., and K. A. Emanuel, 2002: Low frequency variability of tropical cyclone potential intensity 1. Interannual to interdecadal variability. *J. Geophys. Res.*, **107**, 4801, <https://doi.org/10.1029/2001JD000776>.
- Bretherton, C. S., J. R. McCaa, and H. Grenier, 2004: A new parameterization for shallow cumulus convection and its application to marine subtropical cloud-topped boundary layers. Part I: Description and 1D results. *Mon. Wea. Rev.*, **132**, 864–882, [https://doi.org/10.1175/1520-0493\(2004\)132<0864:ANPFSC>2.0.CO;2](https://doi.org/10.1175/1520-0493(2004)132<0864:ANPFSC>2.0.CO;2).



- Camargo, S. J., 2013: Global and regional aspects of tropical cyclone activity in the CMIP5 models. *J. Climate*, **26**, 9880–9902, <https://doi.org/10.1175/JCLI-D-12-00549.1>.
- , and A. H. Sobel, 2004: Formation of tropical storms in an atmospheric general circulation model. *Tellus*, **56A**, 56–67, <https://doi.org/10.3402/tellusa.v56i1.14387>.
- , and A. G. Barnston, 2009: Experimental dynamical seasonal forecasts of tropical cyclone activity at IRI. *Wea. Forecasting*, **24**, 472–491, <https://doi.org/10.1175/2008WAF2007099.1>.
- , and A. A. Wing, 2016: Tropical cyclones in climate models. *Wiley Interdiscip. Rev.: Climate Change*, **7**, 211–237, <https://doi.org/10.1002/wcc.373>.
- , A. G. Barnston, and S. E. Zebiak, 2005: A statistical assessment of tropical cyclone activity in atmospheric general circulation models. *Tellus*, **57A**, 589–604, <https://doi.org/10.3402/tellusa.v57i4.14705>.
- , A. H. Sobel, A. G. Barnston, and K. A. Emanuel, 2007: Tropical cyclone genesis potential index in climate models. *Tellus*, **59A**, 428–443, <https://doi.org/10.1111/j.1600-0870.2007.00238.x>.
- , M. K. Tippett, A. H. Sobel, G. A. Vecchi, and M. Zhao, 2014: Testing the performance of tropical cyclone genesis indices in future climates using the HiRAM model. *J. Climate*, **27**, 9171–9196, <https://doi.org/10.1175/JCLI-D-13-00505.1>.
- , A. H. Sobel, A. D. Del Genio, J. A. Jonas, M. Kelley, Y. Lu, D. A. Shaevitz, and N. Henderson, 2016: Tropical cyclones in the GISS ModelE2. *Tellus*, **68A**, 31494, <https://doi.org/10.3402/tellusa.v68.31494>.
- Delworth, T. L., and Coauthors, 2012: Simulated climate and climate change in the GFDL CM2.5 high-resolution coupled climate model. *J. Climate*, **25**, 2755–2781, <https://doi.org/10.1175/JCLI-D-11-00316.1>.
- DeMaria, M., and J. Kaplan, 1994: A Statistical Hurricane Intensity Prediction Scheme (SHIPS) for the Atlantic basin. *Wea. Forecasting*, **9**, 209–220, [https://doi.org/10.1175/1520-0434\(1994\)009<0209:ASHIPS>2.0.CO;2](https://doi.org/10.1175/1520-0434(1994)009<0209:ASHIPS>2.0.CO;2).
- , M. Mainelli, L. K. Shay, J. A. Knaff, and J. Kaplan, 2005: Further improvements to the Statistical Hurricane Intensity Prediction Scheme (SHIPS). *Wea. Forecasting*, **20**, 531–543, <https://doi.org/10.1175/WAF862.1>.
- Duvel, J.-P., S. J. Camargo, and A. H. Sobel, 2017: Role of the convection scheme in modeling initiation and intensification of tropical depressions over the North Atlantic. *Mon. Wea. Rev.*, **145**, 1495–1509, <https://doi.org/10.1175/MWR-D-16-0201.1>.
- Dvorak, V. F., 1975: Tropical cyclone intensity analysis and forecasting from satellite imagery. *Mon. Wea. Rev.*, **103**, 420–430, [https://doi.org/10.1175/1520-0493\(1975\)103<0420:TCIAAF>2.0.CO;2](https://doi.org/10.1175/1520-0493(1975)103<0420:TCIAAF>2.0.CO;2).
- Emanuel, K. A., 1988: The maximum intensity of hurricanes. *J. Atmos. Sci.*, **45**, 1143–1155, [https://doi.org/10.1175/1520-0469\(1988\)045<1143:TMIOH>2.0.CO;2](https://doi.org/10.1175/1520-0469(1988)045<1143:TMIOH>2.0.CO;2).
- , 2010: Tropical cyclone activity downscaled from NOAA-CIRES reanalysis, 1908–1958. *J. Adv. Model. Earth Syst.*, **2**, <https://doi.org/10.3894/JAMES.2010.2.1>.
- , and D. S. Nolan, 2004: Tropical cyclone activity and the global climate system. *26th Conf. on Hurricanes and Tropical Meteorology*, Miami, FL, Amer. Meteor. Soc., 10A.2, <http://ams.confex.com/ams/pdfpapers/75463.pdf>.
- Gray, W. M., 1979: Hurricanes: Their formation, structure and likely role in the tropical circulation. *Meteorology over the Tropical Oceans*, D. B. Shaw, Ed., Royal Meteorological Society, 155–218.
- Hack, J. J., and W. H. Schubert, 1986: Nonlinear response of atmospheric vortices to heating by organized cumulus convection. *J. Atmos. Sci.*, **43**, 1559–1573, [https://doi.org/10.1175/1520-0469\(1986\)043<1559:NROAVT>2.0.CO;2](https://doi.org/10.1175/1520-0469(1986)043<1559:NROAVT>2.0.CO;2).
- Held, I. M., and M. Zhao, 2011: The response of tropical cyclone statistics to an increase in CO<sub>2</sub> with fixed sea surface temperatures. *J. Climate*, **24**, 5353–5364, <https://doi.org/10.1175/JCLI-D-11-00050.1>.
- Holland, G. J., 1980: An analytic model for the wind and pressure profiles in hurricanes. *Mon. Wea. Rev.*, **108**, 1212–1218, [https://doi.org/10.1175/1520-0493\(1980\)108<1212:AAMOTW>2.0.CO;2](https://doi.org/10.1175/1520-0493(1980)108<1212:AAMOTW>2.0.CO;2).
- , 2008: A revised hurricane pressure–wind model. *Mon. Wea. Rev.*, **136**, 3432–3445, <https://doi.org/10.1175/2008MWR2395.1>.
- Kaplan, J., and M. DeMaria, 2003: Large-scale characteristics of rapidly intensifying tropical cyclones in the North Atlantic basin. *Wea. Forecasting*, **18**, 1093–1108, [https://doi.org/10.1175/1520-0434\(2003\)018<1093:LCORIT>2.0.CO;2](https://doi.org/10.1175/1520-0434(2003)018<1093:LCORIT>2.0.CO;2); Corrigendum, **19**, 482, [https://doi.org/10.1175/1520-0434\(2004\)019<0482:C>2.0.CO;2](https://doi.org/10.1175/1520-0434(2004)019<0482:C>2.0.CO;2).
- Kim, D., A. H. Sobel, A. D. Del Genio, Y. Chen, S. J. Camargo, M.-S. Yao, M. Kelley, and L. Nazarenko, 2012: The tropical subseasonal variability simulated in the NASA GISS general circulation model. *J. Climate*, **25**, 4641–4659, <https://doi.org/10.1175/JCLI-D-11-00447.1>.
- Kim, H.-S., G. A. Vecchi, T. R. Knutson, W. G. Anderson, T. L. Delworth, A. Rosati, F. Zeng, and M. Zhao, 2014: Tropical cyclone simulation and response to CO<sub>2</sub> doubling in the GFDL CM2.5 high-resolution coupled climate model. *J. Climate*, **27**, 8034–8054, <https://doi.org/10.1175/JCLI-D-13-00475.1>.
- Kimball, S. K., and M. S. Mulekar, 2004: A 15-year climatology of North Atlantic tropical cyclones. Part I: Size parameters. *J. Climate*, **17**, 3555–3575, [https://doi.org/10.1175/1520-0442\(2004\)017<3555:AYCONA>2.0.CO;2](https://doi.org/10.1175/1520-0442(2004)017<3555:AYCONA>2.0.CO;2).
- Knaff, J. A., and R. M. Zehr, 2007: Reexamination of tropical cyclone wind–pressure relationships. *Wea. Forecasting*, **22**, 71–88, <https://doi.org/10.1175/WAF965.1>.
- Knutson, T. R., and Coauthors, 2010: Tropical cyclones and climate change. *Nat. Geosci.*, **3**, 157–163, <https://doi.org/10.1038/ngeo779>.
- Kossin, J. P., 2015: Hurricane wind–pressure relationship and eyewall replacement cycles. *Wea. Forecasting*, **30**, 177–181, <https://doi.org/10.1175/WAF-D-14-00121.1>.
- , and S. J. Camargo, 2009: Hurricane track variability and secular potential intensity trends. *Climatic Change*, **97**, 329–337, <https://doi.org/10.1007/s10584-009-9748-2>.
- Lim, Y.-K., S. D. Schubert, O. Reale, M.-I. Lee, A. M. Molod, and M. J. Suarez, 2015: Sensitivity of tropical cyclones to parameterized convection in the NASA GEOS-5 model. *J. Climate*, **28**, 551–573, <https://doi.org/10.1175/JCLI-D-14-00104.1>.
- Lin, S.-J., 2004: A “vertically Lagrangian” finite-volume dynamical core for global models. *Mon. Wea. Rev.*, **132**, 2293–2307, [https://doi.org/10.1175/1520-0493\(2004\)132<2293:AVLFDG>2.0.CO;2](https://doi.org/10.1175/1520-0493(2004)132<2293:AVLFDG>2.0.CO;2).
- Manabe, S., J. L. Holloway Jr., and H. M. Stone, 1970: Tropical circulation in a time-integration of a global model of the atmosphere. *J. Atmos. Sci.*, **27**, 580–613, [https://doi.org/10.1175/1520-0469\(1970\)027<0580:TCIATI>2.0.CO;2](https://doi.org/10.1175/1520-0469(1970)027<0580:TCIATI>2.0.CO;2).
- Manganello, J. V., and Coauthors, 2012: Tropical cyclone climatology in a 10-km global atmospheric GCM: Toward weather-resolving climate modeling. *J. Climate*, **25**, 3867–3893, <https://doi.org/10.1175/JCLI-D-11-00346.1>.
- , and Coauthors, 2014: Future changes in the western North Pacific tropical cyclone activity projected by a multidecadal simulation with a 16-km global atmospheric GCM. *J. Climate*, **27**, 7622–7646, <https://doi.org/10.1175/JCLI-D-13-00678.1>.
- Menkes, C. E., M. Lengaigne, P. Marchesio, N. C. Jourdain, E. M. Vincent, J. Lefèvre, F. Chauvin, and J.-F. Royer, 2012:

- Comparison of tropical cyclogenesis indices on seasonal to interannual timescales. *Climate Dyn.*, **38**, 301–321, <https://doi.org/10.1007/s00382-011-1126-x>.
- Moorthi, S., and M. J. Suarez, 1992: Relaxed Arakawa–Schubert: A parameterization of moist convection for general circulation models. *Mon. Wea. Rev.*, **120**, 978–1002, [https://doi.org/10.1175/1520-0493\(1992\)120<0978:RASAP0>2.0.CO;2](https://doi.org/10.1175/1520-0493(1992)120<0978:RASAP0>2.0.CO;2).
- Murakami, H., and Coauthors, 2012a: Future changes in tropical cyclone activity projected by the new high-resolution MRI-AGCM. *J. Climate*, **25**, 3237–3260, <https://doi.org/10.1175/JCLI-D-11-00415.1>.
- , R. Mizuta, and E. Shindo, 2012b: Future changes in tropical cyclone activity project by multi-physics and multi-SST ensemble experiments using 60-km-mesh MRI-AGCM. *Climate Dyn.*, **39**, 2569–2584, <https://doi.org/10.1007/s00382-011-1223-x>.
- , and Coauthors, 2015: Simulation and prediction of category 4 and 5 hurricanes in the high-resolution GFDL HiFLOR coupled climate model. *J. Climate*, **28**, 9058–9079, <https://doi.org/10.1175/JCLI-D-15-0216.1>.
- , G. Villarini, G. A. Vecchi, W. Zhang, and R. Gudgel, 2016: Statistical–dynamical seasonal forecast of North Atlantic and U.S. landfalling tropical cyclones using the high-resolution GFDL FLOR coupled model. *Mon. Wea. Rev.*, **144**, 2101–2123, <https://doi.org/10.1175/MWR-D-15-0308.1>.
- Nolan, D. S., Y. Moon, and D. P. Stern, 2007: Tropical cyclone intensification from asymmetric convection: Energetics and efficiency. *J. Atmos. Sci.*, **64**, 3377–3405, <https://doi.org/10.1175/JAS3988.1>.
- Putman, W. M., and S.-J. Lin, 2007: Finite-volume transport on various cubed-sphere grids. *J. Comput. Phys.*, **227**, 55–78, <https://doi.org/10.1016/j.jcp.2007.07.022>.
- Reed, K. A., and C. Jablonowski, 2011: Impact of physical parameterizations on idealized tropical cyclones in the Community Atmosphere Model. *Geophys. Res. Lett.*, **38**, L04805, <https://doi.org/10.1029/2010GL046297>.
- , J. T. Bacmeister, N. A. Rosenbloom, M. F. Wehner, S. C. Bates, P. H. Lauritzen, J. E. Truesdale, and C. Hannay, 2015: Impact of the dynamical core on the direct simulation of tropical cyclones in a high-resolution global model. *Geophys. Res. Lett.*, **42**, 3603–3608, <https://doi.org/10.1002/2015GL063974>.
- Roberts, M. J., and Coauthors, 2015: Tropical cyclones in the UPSCALE ensemble of high-resolution global climate models. *J. Climate*, **28**, 574–596, <https://doi.org/10.1175/JCLI-D-14-00131.1>.
- Schubert, W. H., and J. J. Hack, 1982: Inertial stability and tropical cyclone development. *J. Atmos. Sci.*, **39**, 1687–1697, [https://doi.org/10.1175/1520-0469\(1982\)039<1687:ISATCD>2.0.CO;2](https://doi.org/10.1175/1520-0469(1982)039<1687:ISATCD>2.0.CO;2).
- Shaevitz, D. A., and Coauthors, 2014: Characteristics of tropical cyclones in high-resolution models in the present climate. *J. Adv. Model. Earth Syst.*, **6**, 1154–1172, <https://doi.org/10.1002/2014MS000372>.
- Shapiro, L. J., and H. E. Willoughby, 1982: The response of balanced hurricanes to local sources of heat and momentum. *J. Atmos. Sci.*, **39**, 378–394, [https://doi.org/10.1175/1520-0469\(1982\)039<0378:TROBHT>2.0.CO;2](https://doi.org/10.1175/1520-0469(1982)039<0378:TROBHT>2.0.CO;2).
- Sobel, A. H., S. J. Camargo, T. M. Hall, C.-Y. Lee, M. K. Tippett, and A. A. Wing, 2016: Human influence on tropical cyclone intensity. *Science*, **353**, 242–246, <https://doi.org/10.1126/science.aaf6574>.
- Stan, C., 2012: Is cumulus convection the concertmaster of tropical cyclone activity in the Atlantic? *Geophys. Res. Lett.*, **39**, L19716, <https://doi.org/10.1029/2012GL053449>.
- Ting, M., S. J. Camargo, C. Li, and Y. Kushnir, 2015: Natural and forced North Atlantic hurricane potential intensity change in CMIP5 models. *J. Climate*, **28**, 3926–3942, <https://doi.org/10.1175/JCLI-D-14-00520.1>.
- Tippett, M. K., S. J. Camargo, and A. H. Sobel, 2011: A Poisson regression index for tropical cyclone genesis and the role of large-scale vorticity in genesis. *J. Climate*, **24**, 2335–2357, <https://doi.org/10.1175/2010JCLI3811.1>.
- Vecchi, G. A., and B. J. Soden, 2007: Effect of remote sea surface temperature change on tropical cyclone potential intensity. *Nature*, **450**, 1066–1070, <https://doi.org/10.1038/nature06423>.
- , and Coauthors, 2014: On the seasonal forecasting of regional tropical cyclone activity. *J. Climate*, **27**, 7994–8016, <https://doi.org/10.1175/JCLI-D-14-00158.1>.
- Vitart, F. D., and T. N. Stockdale, 2001: Seasonal forecasting of tropical storms using coupled GCM integrations. *Mon. Wea. Rev.*, **129**, 2521–2537, [https://doi.org/10.1175/1520-0493\(2001\)129<2521:SFOTSU>2.0.CO;2](https://doi.org/10.1175/1520-0493(2001)129<2521:SFOTSU>2.0.CO;2).
- , J. L. Anderson, and W. F. Stern, 1997: Simulation of interannual variability of tropical storm frequency in an ensemble of GCM integrations. *J. Climate*, **10**, 745–760, [https://doi.org/10.1175/1520-0442\(1997\)010<0745:SOIVOT>2.0.CO;2](https://doi.org/10.1175/1520-0442(1997)010<0745:SOIVOT>2.0.CO;2).
- , —, J. Sirutis, and R. E. Tuleya, 2001: Sensitivity of tropical storms simulated by a general circulation model to changes in cumulus parametrization. *Quart. J. Roy. Meteor. Soc.*, **127**, 25–51, <https://doi.org/10.1002/qj.49712757103>.
- , A. Leroy, and M. C. Wheeler, 2010: A comparison of dynamical and statistical predictions of weekly tropical cyclone activity in the Southern Hemisphere. *Mon. Wea. Rev.*, **138**, 3671–3682, <https://doi.org/10.1175/2010MWR3343.1>.
- Walsh, K. J. E., and Coauthors, 2016: Tropical cyclones and climate change. *Wiley Interdiscip. Rev.: Climate Change*, **7**, 65–89, <https://doi.org/10.1002/wcc.371>.
- Wehner, M. F., Prabhat, K. A. Reed, D. Stone, W. D. Collins, J. Bacmeister, 2015: Resolution dependence on future tropical cyclone projections of CAM5.1 in the U.S. CLIVAR Hurricane Working Group idealized configurations. *J. Climate*, **28**, 3905–3925, <https://doi.org/10.1175/JCLI-D-14-00311.1>.
- , K. A. Reed, and C. M. Zarzycki, 2017: High-resolution multi-decadal simulation of tropical cyclones. *Hurricanes and Climate Change*, J. M. Collins and K. Walsh, Eds., Springer International Publishing, 187–211.
- Wing, A. A., A. H. Sobel, and S. J. Camargo, 2007: Relationship between the potential and actual intensities of tropical cyclones on interannual time scales. *Geophys. Res. Lett.*, **34**, L08810, <https://doi.org/10.1029/2006GL028581>.
- Zarzycki, C. M., K. A. Reed, J. T. Bacmeister, A. P. Craig, S. C. Bates, and N. A. Rosenbloom, 2016: Impact of surface coupling grids on tropical cyclone extremes in high-resolution atmospheric simulations. *Geosci. Model Dev.*, **9**, 779–788, <https://doi.org/10.5194/gmd-9-779-2016>.
- Zhang, W., and Coauthors, 2016: Improved simulation of tropical cyclone responses to ENSO in the western North Pacific in the high-resolution GFDL HiFLOR coupled climate model. *J. Climate*, **29**, 1391–1415, <https://doi.org/10.1175/JCLI-D-15-0475.1>.
- Zhao, M., I. M. Held, S.-J. Lin, and G. A. Vecchi, 2009: Simulations of global hurricane climatology, interannual variability, and response to global warming using a 50-km resolution GCM. *J. Climate*, **22**, 6653–6678, <https://doi.org/10.1175/2009JCLI3049.1>.
- , —, and —, 2012: Some counterintuitive dependencies of tropical cyclone frequency on parameters in a GCM. *J. Atmos. Sci.*, **69**, 2272–2283, <https://doi.org/10.1175/JAS-D-11-0238.1>.